

ERUPTION OF A MULTIPLE-TURN HELICAL MAGNETIC FLUX TUBE IN A LARGE FLARE: EVIDENCE FOR EXTERNAL AND INTERNAL RECONNECTION THAT FITS THE BREAKOUT MODEL OF SOLAR MAGNETIC ERUPTIONS

G. ALLEN GARY AND R. L. MOORE

Marshall Space Flight Center, SD50, Huntsville, AL 35812; allen.gary@nasa.gov, ron.moore@nasa.gov

Received 2003 November 26; accepted 2004 April 21

ABSTRACT

We present observations and an interpretation of a unique multiple-turn spiral flux tube eruption from active region 10030 on 2002 July 15. The *TRACE* C IV observations clearly show a flux tube that is helical and erupting from within a sheared magnetic field. These observations are interpreted in the context of the breakout model for magnetic field explosions. The initiation of the helix eruption, as determined by a linear backward extrapolation, starts 25 s after the peak of the flare’s strongest impulsive spike of microwave gyrosynchrotron radiation early in the flare’s explosive phase, implying that the sheared core field is not the site of the initial reconnection. Within the quadrupolar configuration of the active region, the external and internal reconnection sites are identified in each of two consecutive eruptive flares that produce a double coronal mass ejection (CME). The first external breakout reconnection apparently releases an underlying sheared core field and allows it to erupt, leading to internal reconnection in the wake of the erupting helix. This internal reconnection releases the helix and heats the two-ribbon flare. These events lead to the first CME and are followed by a second breakout that initiates a second and larger halo CME. The strong magnetic shear in the region is compatible with the observed rapid proper motion and evolution of the active region. The multiple-turn helix originates from above a sheared-field magnetic inversion line within a filament channel, and starts to erupt only after fast breakout reconnection has started. These observations are counter to the standard flare model and support the breakout model for eruptive flare initiation.

Subject headings: Sun: activity — Sun: corona — Sun: coronal mass ejections (CMEs) — Sun: flares — Sun: magnetic fields

La représenter avec une structure spirale — P. A. Secchi¹

1. INTRODUCTION

The complex event and structures of the X3 solar flare of 2002 July 15, 20:04 UT, have been discussed in a recent Letter by Liu et al. (2003) in the context of an erupting flux rope model. In Figure 1 a set of six 160 nm images from *TRACE* show the eruption of a multiple-turn helical field in the flare. These images captured the ejection of a multiple-turn helical flux tube from a sheared magnetic field, which is required by and is a major signature of the standard model of eruptive flares (EFs). However, here we find this event, which produced a fast coronal mass ejection (CME), to have all the features required by the breakout model of magnetic field explosions. This model is compatible with the erupting helix because the helix represents a unique instance of an eruption of a low-lying highly sheared magnetic field, which is a central requirement of both the standard and breakout models, as well as of many other flare models (i.e., Moore et al. 2001; DeVore & Antiochos 2000; Forbes & Priest 1995; Priest & Milne 1980; Birn & Schindler 1981; Hood & Priest 1980). Significantly, we observe that the “breakout” of remote flare brightening occurs before the “explosion” of the sheared and helical core magnetic field. This observation favors the breakout model for the initiation of this flare.

It is generally recognized that CMEs/EFs are part of a single complex phenomenon that includes (1) stressed magnetic

fields, (2) a triggering event(s) for rapid reconnection, (3) the eruption of the magnetic field, and (4) the postflare closure of the field. The least understood of all the components of CMEs/EFs is the triggering mechanism that switches on rapid reconnection. At the center of the various models explaining CME/EF events, but playing different roles, is a stressed magnetic field requiring magnetic helicity. The observation of helicity has become a prominent part of solar physics in the last decade. The new, time-dependent, three-dimensional magnetohydrodynamics codes show specifically how a sheared magnetic field can form multiple-turn core fields of filaments (DeVore & Antiochos 2000).

The concept of twisted coronal loops has played an important part in modeling solar phenomena (e.g., Anzer & Tandberg-Hanssen 1970; Rust & Kumar 1996; Sturrock et al. 1984; van Ballegooijen & Martens 1989, 1990; Amari et al. 1996, 1999, 2003; Antiochos et al. 1999; Aulanier et al. 2000; Moore et al. 2001; Lionello et al. 2002). Now, with the *TRACE* observations reported herein, we have an excellent example of a core field erupting from the site of a sheared photospheric magnetic field and a chromospheric filament. In addition to the mechanism of DeVore & Antiochos (2000), which involves reconnection up in the body of the progressively sheared magnetic arcade, there are two other possible mechanisms (Lionello et al. 2002) that can create a preflare flux-rope configuration: either magnetic flux cancellation in the photosphere (van Ballegooijen & Martens 1989; Amari et al. 1996, 1999) or emergence of a flux rope from below the photosphere (van Ballegooijen & Martens 1990). The

¹ Secchi (1870, p. 197) reports an observation by Major James Francis Tennant of a spiral structure prominence in the corona during the total eclipse of 1860 June 18.

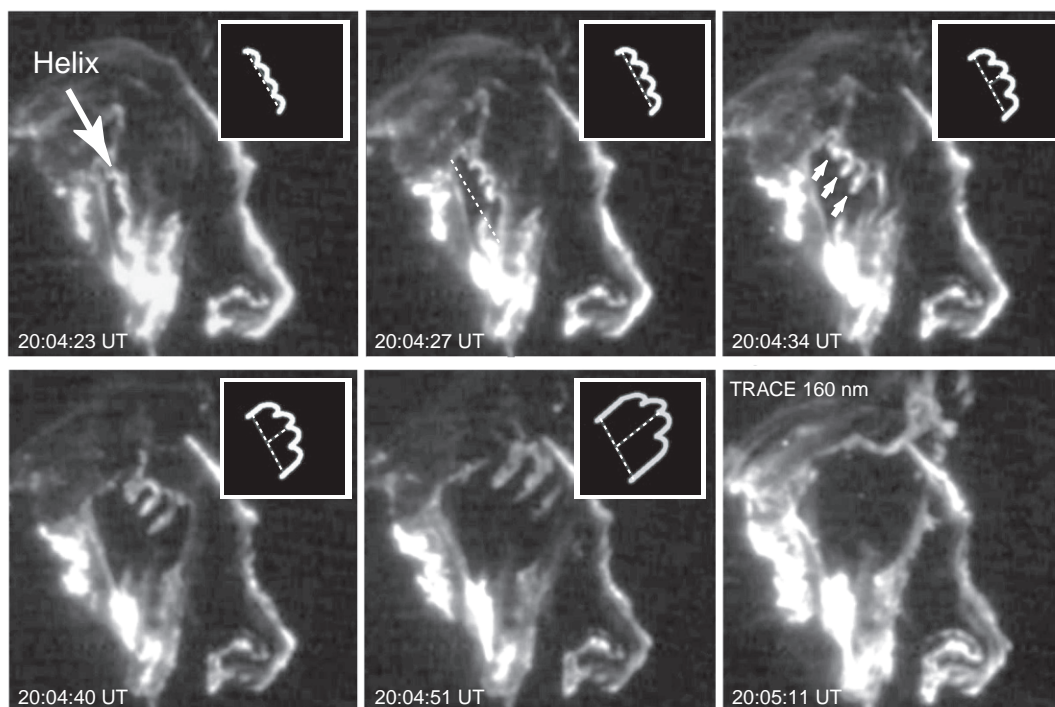


FIG. 1.—Multiple-turn helix in the X3 flare of 2002 July 15. The helix arises from the sheared magnetic field along the neutral line between two flare ribbons at the feet of the helix. The emission is from C iv. The *TRACE* 160 nm image has a field of view of $125''$ located between the positive sunspots P_1 and P_3 (see Fig. 2 of AR 10030). The eruption starts at $\sim 20:04:17$ UT and accelerates at 25 km s^{-1} during the first 30 s. The helix clearly has three turns at 20:04:51 UT, and these are seen earlier in the eruption (see the white arrows at 20:04:34 UT). In the movie version of this eruption, containing 39 frames taken every 2 s, both legs of the helix are seen, with the leg to the southwest showing an untwisting action. The base length of the helix is $3.9 \times 10^4 \text{ km}$ as measured from foot to foot. From 20:04:51 UT, the loop begins to disappear, and identification of the turns is impossible. A simple model of an erupting helix of three turns simulates the observed helix during the time period of 20:04:23–20:04:51 UT. Shown with the same appropriate aspect angle as the C iv observations of the helix eruption, this simulation has the bowed helix core rising with each leg of the flux tube fixed to a photospheric footpoint. An unwinding model can reproduce the spinning motion of the legs of the helix, as seen in the southwestern leg of the *TRACE* helix.

flux rope might then erupt through any of three mechanisms: (1) loss of equilibrium via flux-cancellation reconnection through convergence or diffusion (van Ballegoijen & Martens 1989; Amari et al. 1999, 2003), (2) tether-cutting reconnection (Sturrock et al. 1984; Moore et al. 2001), or (3) breakout reconnection (Antiochos et al. 1999; Aulanier et al. 2000; Sterling et al. 2001; Maia et al. 2003). Hence, in the literature there are several mechanisms that could form a pre-eruptive flux rope and several mechanisms that could cause it to erupt. Our observations do not show whether the helical flux rope was formed before it erupted, but the timing and the magnetic location of the flare brightenings before the helix started to erupt clearly indicate that the eruption was released via a breakout reconnection associated with a null above the helix.²

The helical flux tube is plainly defined in the *TRACE* rapid sequence of 16 images (cf. Liu et al. 2003). This clearly represents the creation of a helical field either before the eruption (e.g., DeVore & Antiochos 2000) or the during the eruption via core-field tether-cutting reconnection (Moore et al. 2001). Large-scale helical structures associated with CMEs have been inferred to be ubiquitous in pre-eruptive and eruptive prominences (Dere et al. 1999; DeVore & Antiochos 2000; Moore et al. 2001). The main point of the observations, which are discussed in further detail below, is that the initiation of the helix eruption starts some 25 s after the first peak of the impulsive-phase microwave gyrosynchrotron radiation,

implying that the eruptive core field was not the initial reconnection/acceleration site. In Figure 2 the general magnetic field configuration is seen in the Marshall Space Flight Center (MSFC) vector magnetogram (*top*, with the main components of the active region labeled) and in a Michelson Doppler Imager (MDI) longitudinal magnetogram (*bottom*). This labeling is referred to throughout the paper. In Figure 3 the site of the helix eruption is seen to be the site of a filament in a preflare $H\alpha$ image. The filament is along the center north-south neutral line, the inversion line of the longitudinal magnetic field, labeled L_b in Figure 2. The image in Figure 3 also shows the general complexity of the region.

Again, the important finding of this paper is that these observations are counter to the standard flare model and support the breakout model for the eruption onset. However, these observations do not rule out reconnection within a sheared magnetic arcade yielding the helical field lines during the onset of eruption. As we follow the events in the quadrupolar configuration of the active region, we identify the internal and external reconnection sites that are associated with a double-flare event and a double CME. External breakout reconnection begins before the helix eruption and before the internal reconnection below it. These events give rise to a CME. After the field that opens in this CME recloses, a second episode of external breakout reconnection initiates a second and stronger halo CME. The strong magnetic shear of the region is associated with rapid proper motion and evolution of the active region. The multiple-turn helix originates from above a magnetic inversion line in the sheared magnetic field

² For movies of the region, see <http://science.nasa.gov/ssl/PAD/SOLAR/papers/garyga/HelixPaper.html>.

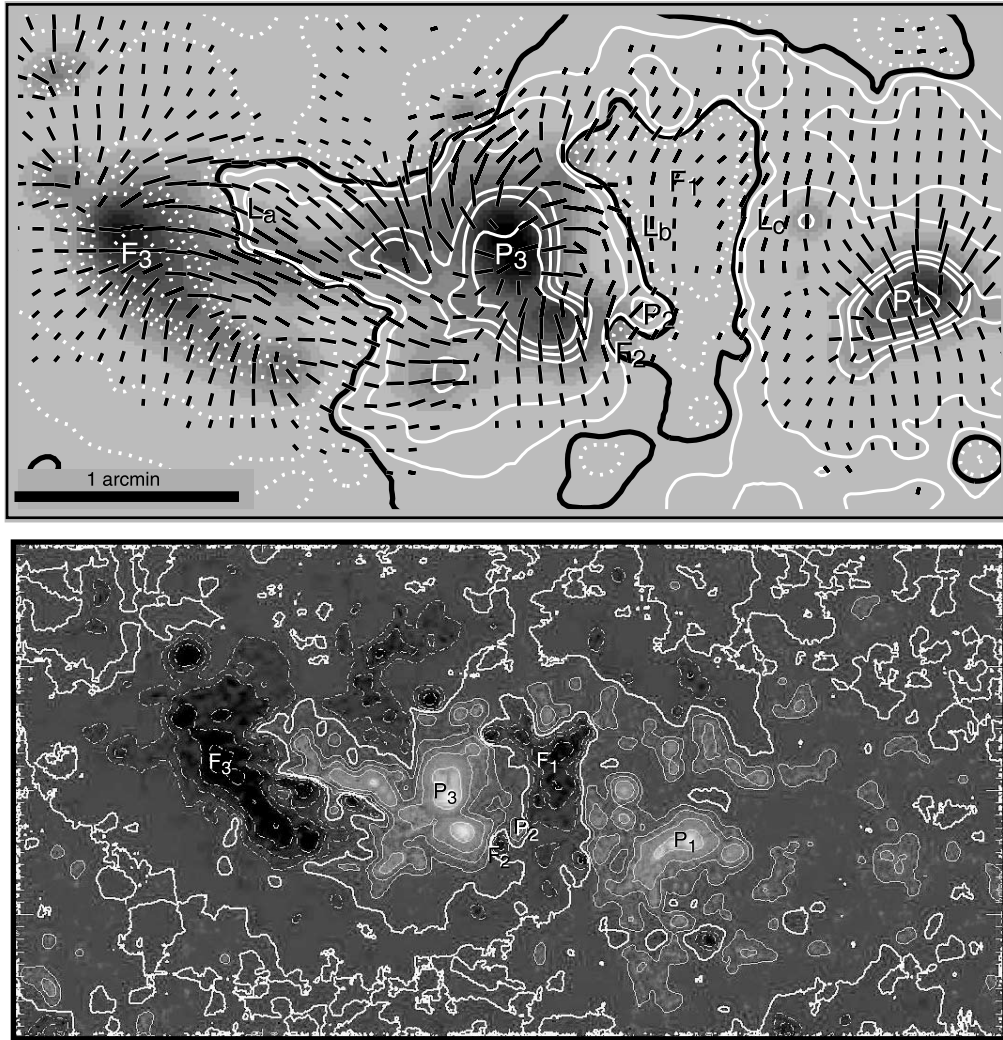


FIG. 2.—*Top*: MSFC vector magnetogram of AR 10030 showing the nonpotential field along the three main neutral-line segments L_a , L_b , and L_c . The magnetic contour levels are ± 2000 , 1500, 1250, 1000, 200, 50, and 0 G. The transverse field vectors are shown as dashes. The magnetic field along these neutral-line segments is strongly sheared, having departure angles from the potential field greater than 45° (Falconer et al. 2002). The photospheric brightness is the background image. The images of Fig. 1 are about one-fourth the width of this magnetogram and center on F_1 . *Bottom*: High-resolution MDI magnetogram (10:56 UT) showing the principal sunspots, magnetic islands, and neutral lines. The small bipolar delta region (P_2 and F_2) developed during the day of July 15. The second, lower sunspot of P_3 moved rapidly (0.19 km s^{-1}) to the west during the day with respect to the main spot of P_3 . The MDI image magnetograms show motion of F_3 to the east. The motion within the complex continuously changes the stressed global magnetic field. The field of view is 4.35×8.72 .

in a filament channel but starts to erupt only well after breakout has been initiated.

Section 2 of this paper describes (1) transition region and chromospheric images that show the eruptive helix and the sites of enhanced emission (heating), (2) the photospheric magnetic field, which leads to an understanding of the three-dimensional field configuration, (3) the time profiles of the X-ray and microwave data that mark the events, and (4) the observations of the two CMEs that certify the global magnetic breakout. The many observations from the various solar instruments reveal the nature of the event in detail. Section 3 presents the analysis of the configuration of the magnetic field and characterizes the physical properties of the erupting helix. Section 4 summarizes the analysis and presents a schematic model that fits the observations. In particular, we consider a multiple-turn helical magnetic flux tube within a sheared magnetic field and its context within the breakout model for magnetic field explosions. The roles of external and internal

reconnection in the destabilization of the active region's magnetic field are discussed.

2. OBSERVATIONS

There are ample observations giving the general nature of the magnetic field topology associated with the event. The quadrupolar magnetic components of the region are labeled on the vector magnetogram (Fig. 2), including three sheared-field segments of the magnetic neutral line (L_a , L_b , and L_c). The erupting helix comes from over the neutral line L_b , and flare ribbons occur along each of the two sheared-field neutral lines (L_b and L_c) to the right of the preceding sunspot (P_3).

2.1. Transition Region and Chromospheric Images

On 2002 July 15, the *TRACE* instrument was in a 160 nm flare mode when an X3 X-ray flare in active region 10030 occurred. Details of the *TRACE* instrumentation can be found

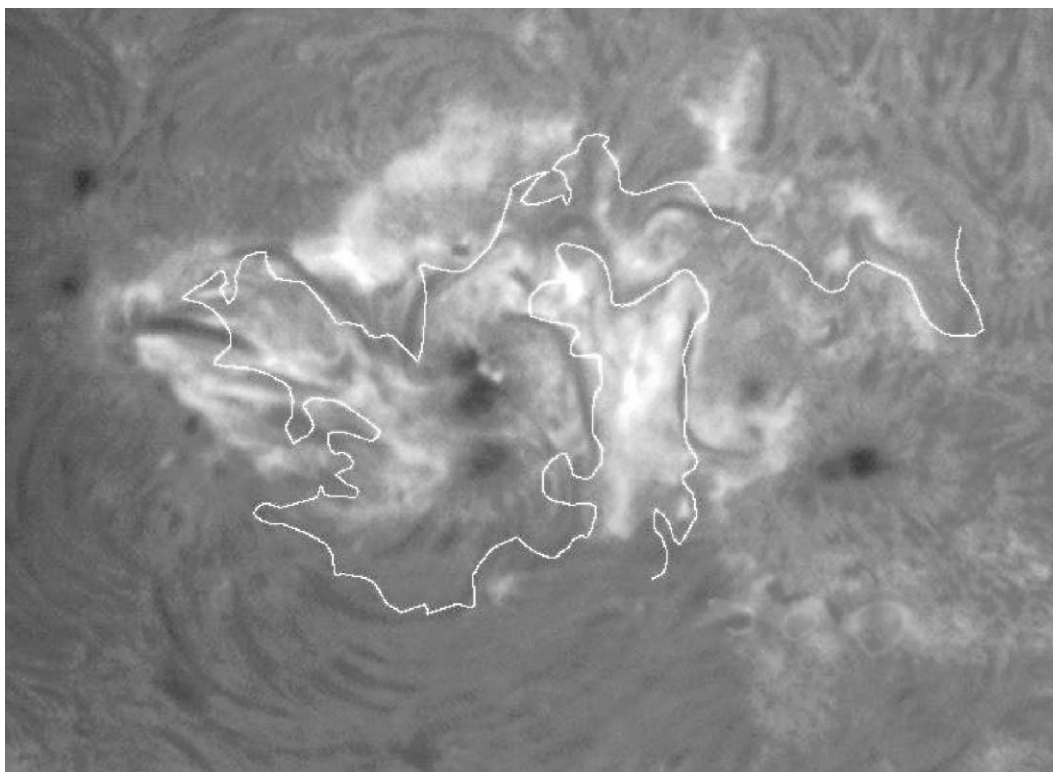


FIG. 3.—SOON Learmonth/Space Environment Center $H\alpha$ image showing the filaments associated with neutral-line segments L_a , L_b , and L_c at 5:42 UT. The continuous neutral line (white line) is obtained from the high-resolution MDI magnetogram (Fig. 2).

in Handy et al. (1999). The active region was observed throughout most of the day in a flare-monitoring mode with a 768×768 pixel detector, with a spatial resolution of $1''$. The total image count for the day was 6005. For the period of 20:00–20:03 UT there are 48 images from the 768×768 pixel detector, and after 20:02:59 UT there are 828 images from a 512×512 pixel detector of spatial resolution $0''.5$ and temporal cadence of every 2 s. The UV continuum 160 nm images capture the two-ribbon flares and other regional brightenings. The spectral response of the 160 nm filter (24.5 nm FWHM) peaks near 155 nm and captures the strong C IV resonant line pair emission ($2s-2p$, 154.82 and 155.08 nm) from the transition region at 100,000 K in the flaring stage; the background quiet-Sun emission is from photoionization of Si ($3p^2\ ^3P$) around the temperature minimum region (Handy et al. 1998; Qiu et al. 2000; Cuny 1971). For an X3 flare, the C IV radiance (specific intensity) brightens by a factor of more than 3400 (Brekke et al. 1996); hence, the C IV emission dominates the emission from 20:03 UT until after 20:30 UT. (We refer herein to these images as C IV images, but these are not the reduced C IV TRACE images obtained by the method of Handy et al. [1998].) During the preflare phase, TRACE captures transient brightenings probably related to flux emergence, flux cancellation, and less dramatic magnetic field restructuring. The images show the helix eruption starting at 20:04 UT, ~ 1 minute into the flare according to the NOAA flare listing. The eruption occurs on the eastern side of the leading spot (P_1). The TRACE team reports that “the region was so bright that TRACE reduced the exposure times to as little as $1/625$ s starting at 20:03 UT; the result is that the background emission disappears entirely and only detector and data-compression noise are seen outside the bright flare kernel for a while, until exposure times become longer than $1/150$ s after 20:07:28 UT.”

In Figure 1 the multiple-turn helix is seen erupting from a site of sheared magnetic field (§ 2.2). The TRACE subarrays shown have a field of view of $125''$ located between the positive sunspots P_1 and P_3 (e.g., Liu et al. 2003). The eruption starts at $\sim 20:04$ UT and accelerates during the first 30 s. The helix clearly has three turns, as seen at 20:04:51 UT; however, at 20:04:34 UT there are indications in the movie of the event that perhaps there are more than three knots in the early phase of the eruption. In the TRACE observations of this eruption, containing 39 frames taken every 2 s, both legs of the helix are seen, with the leg to the southwest showing an untwisting action. The base length of the helix is 3.9×10^4 km as measured from foot to foot. After 20:04:51 UT, the loop begins to disappear, and identification of the turns is impossible.

TRACE C IV images of key events in the X3 flare are shown in Figure 4. The field of view here is $6'.8 \times 6'.8$, i.e., ~ 3 times the field of view of Figure 1. At 19:49:58 and 20:02:53 UT we identify a set of the emission features E_1 , E_2 , E_3 , and E_4 . The first eruption produces the two flare ribbons R_1 (shown at 20:05:02 UT) across the sheared-field neutral line L_b . At 20:28:01, a second eruption produces the two flare ribbons R_2 across the sheared-field neutral line L_c . At 20:28:41 UT, a coronal feature (S) is seen; from the movie it is clear that this feature is in the lower corona. In the later phase of the flare, at 20:41:58 UT, the sites E'_1 and E'_4 brighten again. The main neutral line (thin line) is from the MDI longitudinal magnetogram (Fig. 2, bottom).

Chromospheric images in $H\alpha$ were obtained by the Big Bear Solar Observatory in the preflare time frame and during the flare by the US Air Force Solar Optical Observing Network (SOON) observatories at Holloman Air Force Base and Learmonth, Australia. SOON $H\alpha$ images show remote $H\alpha$ flare brightenings (at E_1 , E_2 , E_3 , and E_4) at 20:02:25 UT,

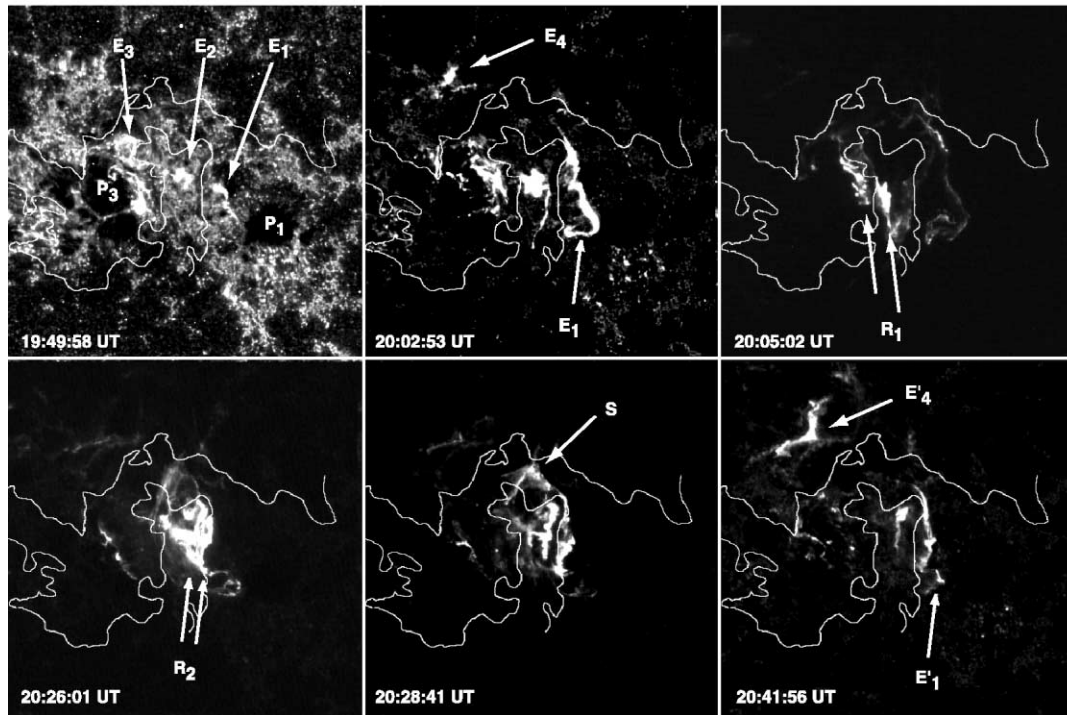


FIG. 4.—*TRACE* 160 nm images of key events in the X3 flare. At 19:49:58 and 20:02:53 UT the emission patches E_1 , E_2 , E_3 , and E_4 are located at separatrix sites. The first eruption produces the two flare ribbons R_1 (shown at 20:05:02 UT) across the sheared-field neutral line L_b . At 20:26:01, a second eruption produces the two flare ribbons R_2 across the sheared-field neutral line L_c . At 20:28:41, an upper atmospheric coronal separatrix (S) is seen. From the movie it is clear that this feature is located in the low corona. In the later phase of the flare, at 20:41:58 UT, the reclosing reconnection of the field again brightens separatrix sites E'_1 and E'_4 . The thin line is the main neutral line from Fig. 2.

near the start of the impulsive phase (in the rise of the microwave peak r_1). Following this, the SOON images show the development of the two-ribbon flare bracketing the neutral line L_b . In Figure 3 a Learmonth $H\alpha$ image (05:42 UT) shows well the filaments associated with neutral-line segments L_a , L_b , and L_c . The filaments of the neutral lines L_b and L_c return after the event; they are seen again early on July 16.

2.2. Vector and Longitudinal Magnetograms

On 2002 July 15, the MSFC solar vector magnetograph obtained a set of magnetograms of AR 10030 that showed strong magnetic shear along the neutral lines. The field of view of the instrument is $7' \times 5.5'$ (328×258 obtained by 2×2 binning of $0''.64$ pixels). Seven vector sets were obtained between 17:18 and 18:03 UT: four sets were taken at 9 pm to the blue of line center, one set was at 9 pm to the red of line center, one set was for photocalibration, and one set was for dark-current calibration (for the data analysis process and reduction methods, see Hagyard et al. 1981, 1998, 1999, 2000; Gary et al. 1987; Ronan et al. 1992 and references therein). Each set has co-aligned $H\alpha$ images. The photospheric vector magnetograms, obtained from the $Fe\ I$ Zeeman line at 525.02 nm, measure the nonpotentiality of the region. In particular, they show the high magnetic shear along the neutral line in the active region.

In Figure 2 the MSFC vector magnetogram shows the strongly sheared nonpotential field along the three segments L_a , L_b , and L_c of the main neutral line. The photospheric magnetic contour levels are ± 1000 , 700, 400, 50, and 10 G. The transverse field vectors are shown as dashes. A highly sheared (shear angle $> 45^\circ$) transverse magnetic field along neutral lines is correlated with CME events (Falconer et al.

2002). In this figure the background is the photospheric brightness in the $Fe\ I$ 525.02 nm line.

On the ESA/NASA *Solar and Heliospheric Observatory* (*SOHO*) satellite, the MDI obtained full-disk longitudinal photospheric magnetograms using the $Ni\ I$ Zeeman line at 676.78 nm (Scherrer et al. 1995). The 1024×1024 , 60 s cadence, full-disk magnetograms, having $4''.0$ spatial resolution and ~ 50 G uncertainty, were used to investigate the dynamic movement of several magnetic features during the day. The full-disk (level 1.5/reformatted and calibrated) images at 60 s cadence were obtained in the time intervals 00:00–05:40, 11:04–12:35, 13:52–13:59, and 14:00–14:28 UT, with additional observations at 16:00, 17:36, 19:12, 20:48, and 22:24 UT. The MDI image magnetograms show eastward motion of F_3 relative to P_3 . This and other motions within the complex continuously change the stressed global magnetic field. MDI also provided high-resolution images of the active region with a $11''.0 \times 11''.0$ field of view and $1''.25$ spatial resolution. For July 15, high-resolution MDI magnetograms were obtained around 10:54 and 13:41 UT. For the high-resolution images, the center of the field was displaced $160''$ to the north of the center of the full-disk field in the usual orientation and captured AR 10030 at $N22^\circ$, $E01^\circ$ on 2002 July 15. In Figure 2 (*bottom*) the high-resolution MDI magnetogram at 10:56 UT shows the details of the principal sunspots, magnetic islands (magnetic flux concentrations of opposite polarity to their surroundings), and neutral lines. A small bipolar delta region (P_2 and F_2) developed at the southern end of L_b during the day of July 15, and at the northern end another small bipolar region developed, as was pointed out by Liu et al. (2003). The second, lower sunspot of P_3 moves rapidly (0.19 km s^{-1}) to the west during the day with respect to the main spot of P_3 .

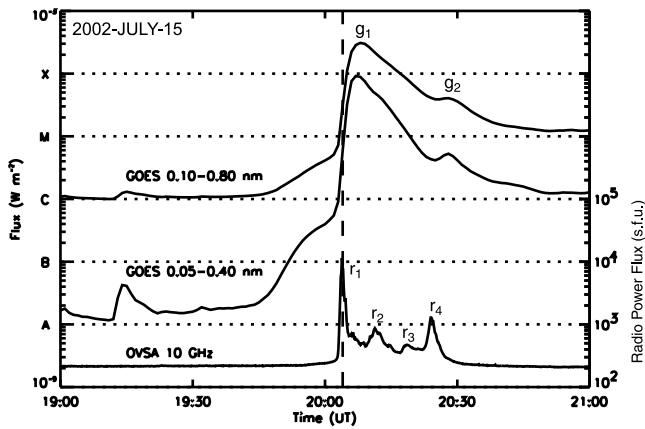


FIG. 5.—Time profiles of the *GOES* X-ray flux in the 0.1–0.8 and 0.05–0.4 nm bands ($\Delta t = 1$ minute) and the *OVSA* 10 GHz microwave power ($\Delta t = 8$ s). The peaks in the X-ray profiles are at g_1 (20:07; X3.1) and g_2 (20:28; M4.1), and the peaks in the radio profile are at r_1 (20:03:52), r_2 (20:11:20), and r_3 (20:24:12). The microwave bursts have a FWHM ~ 2 –4 minutes. A reference line (dashed line) is drawn at 20:04:00 UT.

There are 0^h:12 images and movies of the region from the Swedish 1 m Solar Telescope, but the field of view only captures the sunspot P_3 (Scharmer et al. 2002).

2.3. X-Ray and Microwave Time Profiles

The *Geostationary Operational Environmental Satellite* (*GOES*-8) observed the soft X-ray emission of the X3.1 flare with 1 minute time resolution. The full-disk integrated X-ray flux as a function of time during the time period of 19:00–21:00 UT, observed in the 0.05–0.4 and 0.1–0.8 nm channels, is shown in Figure 5. The main peak (X3.1) at g_1 (20:07 UT) and a secondary peak at g_2 (20:28; M4.1) were produced by the two ejective flare events in AR 10030.

The Owens Valley Solar Array (*OVSA*) obtained multi-frequency microwave emission in the 1–18 GHz range at an 8 s temporal resolution. This microwave emission is gyro-synchrotron radiation that is produced by the same population of electrons that produce the 10–100 keV hard X-ray bremsstrahlung emission in the impulsive phase of flares (Gary 2000). There are four main microwave bursts, occurring at r_1 (20:03:52), r_2 (20:11:20), r_3 (20:18:36), and r_4 (20:24:12 UT), and the bursts have typical FWHM time durations of ~ 2 –4 minutes, as determined from the 10 GHz profile. The *OVSA* 10 GHz microwave power flux is plotted with the *GOES* data in Figure 5.

2.4. Coronagraph Images

Associated with the X3 flare of AR 10030, the *SOHO* LASCO observed the first CME event on July 15 at 20:30 UT and the second CME about a half hour later. The second CME was initially observed as a bright front off the northeast limb and as a full halo CME by 22:30 UT. The halo is fainter in the south and is seen there only in the difference images. The LASCO team reported that the front moved fast (~ 1100 km s^{-1}) and had some trailing material mainly in the northeast. The C2 coronagraph (2 – $6 R_\odot$), with $23''$ spatial resolution, recorded strong CME emission in the northeastern corona between 20:30 and 22:30 UT. The C3 coronagraph (3.7 – $32 R_\odot$) difference images, with $112''$ spatial resolution, show the CME from 21:18 UT (July 15) to 03:18 UT (July 16) as a halo CME. In Figure 6 a difference image shows the

second CME as seen by LASCO C3 at 02:18 UT on July 16. A weak halo is seen opposite the main emission.

2.5. Chronology of Events

According to the *GOES* and *OVSA* time profiles (Fig. 5), the eruption events started at 20:02 UT, with preflare X-ray activity starting at 19:45 UT. Below we list the chronology of the events associated with the July 15 X3 flare, helix eruption, and CME eruptions:

19:45 UT.—Preflare X-ray emission begins.

19:50 UT.—Transition region C iv emission is seen at E_1 , E_2 , E_3 , and E_4 .

20:02 UT.—The X-ray impulsive phase begins with $H\alpha$ ribbons and enhanced C iv brightenings at E_1 , E_2 , E_3 , and E_4 .

20:03:52 UT.—The first microwave burst r_1 from 10–100 keV electrons peaks.

20:04:17 UT.—About 25 s after r_1 peaks, the helix is seen to begin to ascend in the C iv movie. The first set of C iv ribbons (R_1) across L_b start to form.

20:05 UT.—The helix disappears, and flare R_1 ribbons are fully formed in C iv and $H\alpha$.

20:07 UT.—The peak of the *GOES* X-ray flux (X3.1, 0.1–0.8 nm channel) occurs.

20:11:20 UT.—The second microwave burst r_2 from 10–100 keV electrons peaks.

20:18:36 UT.—The third microwave burst r_3 from 10–100 keV electrons peaks.

20:24:12 UT.—The fourth microwave burst r_4 from 10–100 keV electrons peaks.

20:26 UT.—The second set of C iv ribbons (R_2) has formed across L_c , which is a separate site from the first flare ribbons (R_1).

20:28 UT.—The secondary peak of the *GOES* X-ray flux (M4.1, 0.1–0.8 nm channel) occurs.

20:29 UT.—The coronal feature S is seen in C iv.

20:30 UT.—The first CME is seen in LASCO C2 in the northeast.

20:41 UT.—Two remote C iv emission patches (E'_1 and E'_4) have brightened.

22:18 UT.—The second CME is first seen in LASCO C3 difference images.

23:18 UT.—The second CME is seen as a halo event in LASCO C3 difference images.

02:18 UT (July 16).—The second CME reaches $25 R_\odot$ and is seen as a halo event.

3. ANALYSIS

The solar eruptions of July 15 are analyzed in terms of the magnetic configuration and external and internal reconnection. In this section we discuss (1) the magnetic morphology as determined by magnetograms and their extrapolation, (2) a step-by-step scenario of the emissions and timing of the C iv and chromospheric features seen in the data, and (3) the dynamical formation and velocities of the erupting *TRACE* helix. The observation of the eruption of the helix from a sheared core field is of particular importance.

In Figure 1 (*insets*) a simple model of an erupting helix of three turns simulates the time period of 20:04:23–20:04:51 UT. Shown with the same appropriate aspect angle as the C iv observations of the helix eruption, this simulation has a semi-circular-shaped helix rising with the legs of the flux tube fixed to two “photospheric” footpoints. Because of the aspect angle

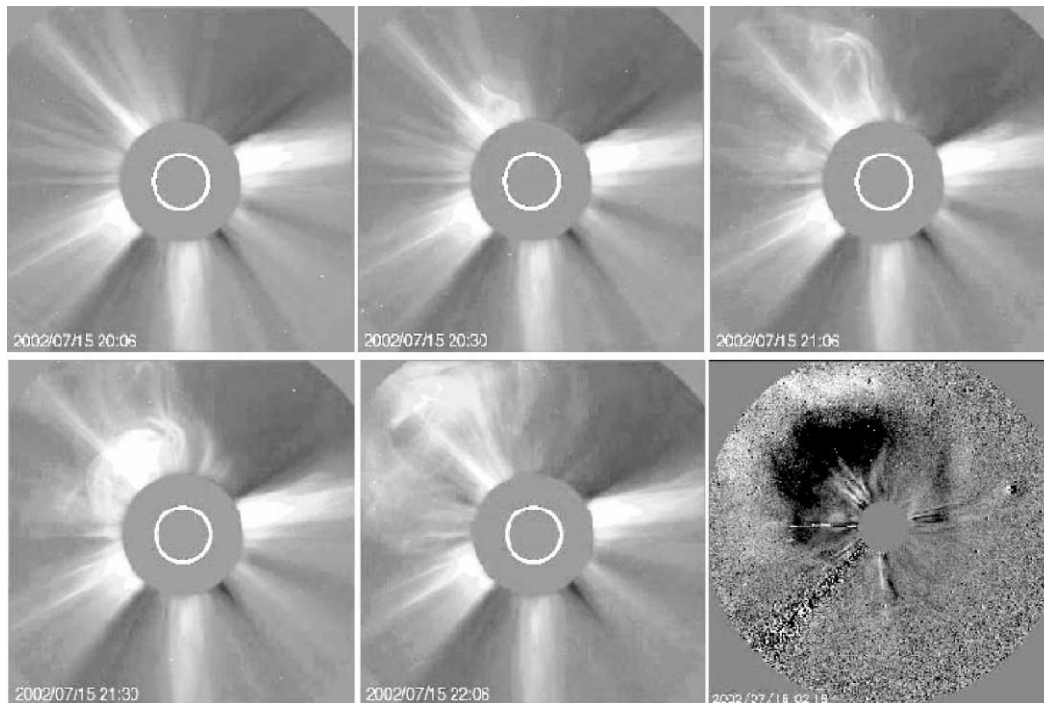


FIG. 6.—Double CME event of July 15, 20:30 UT, produced in tandem with the X3 X-ray flare. Although classified as a halo event, bright fronts are seen in the northeast; the active region location was N22°, E01°. The first CME, the weaker of the two, is seen in the top panels, and the strong second CME is seen in the bottom panels. The full halo of the second CME was observed by 22:06 UT; however, the emission was fainter in the south. The second CME had a fast speed of $\sim 1100 \text{ km s}^{-1}$. In the bottom right panel, a difference image shows the second CME as seen by LASCO C3 at 02:18 UT on July 16. The weak halo in the southeast is seen opposite the main emission in the northeast. The images in the first five panels are nondifferenced LASCO C2 images.

and the bowed central core, each of the loops seen in the insets has a V-cusp shape toward the originating neutral line and a rounded top. The V-cusps are seen in the *TRACE* observations.

3.1. Magnetic Morphology

A set of potential field lines are shown in Figure 7; these were computed from an MDI magnetogram, taking the region viewed in the magnetogram to be a flat plane. The field calculation used the Fourier method of Alissandrakis (1981) with an extended neutral border (8 times the area of the magnetogram) to reduce the periodicity effect on the field lines. The potential field is used to show the topology of the nonpotential quadrupolar complex. A set of field lines (*white lines*) are specifically associated with the region enclosing the negative field of F_1 . The outer extremities of this set of field lines define the separatrix cupola. The influence of the small magnetic delta dipoles (e.g., P_2 and F_2) is negligible on the overall quadrupolar field. The height in the side view is 140 Mm. At this height the plasma β is ~ 1 (Gary 2001); hence, the magnetic field is influenced by the (unknown) upper boundary conditions, and this current-free-field calculation models only the general connectivity to be expected, i.e., the topology (e.g., Aulanier et al. 2000). In particular, the plasma β starts increasing at heights above 1 Mm and approaches a value of 1 in the 10^2 – 10^3 Mm region, and hence the magnetic field in the vicinity of the null is influenced by the plasma β , and this effect is not accounted for by a potential field model (Gary 2001; Gary & Alexander 1999). In addition, the exact conjugate footpoints of the field lines passing near the null are not modeled by this field. However, the low-lying null position given by the potential calculation (seen in Fig. 7 at $h \sim 10^4$ km) is expected to approximately correct for this feature. Moreover, the morphology of the potential field reflects the general

morphology of the region. In Figure 7 (*top*) the set of field lines plotted start on a line that is roughly the axis of symmetry of the region. This model emphasizes the null above the region F_1 by having the field lines associated with F_1 in white. The appropriate upper boundary conditions are unknown and are not included in the calculation. It is probable that breakout reconnection at the null initiates the eruption of the sheared field along the neutral line L_b and, in a second episode, initiates the eruption of the sheared field along the neutral line L_c .

In Figure 8 (*left*) the enlargement shows the *TRACE* image at 20:28:41 UT extracted from Figure 4. Here the shape of the separatrix feature is that of an inverted-Y, located in the corona above the negative region F_3 . From the C IV movie it appears that this feature is not the separatrix of the potential field but is generated at the base of the reclosing-reconnection current sheet in the wake of the second eruption. This separatrix region appears to be filled with material from the eruption that produces the second two-ribbon flare. An illustration of the event is shown in Figure 8 (*right*), with a set of field lines defining the separatrix. Filippov (1999) points out that null points are usually assumed to be sites of reconnection. However, in an observation of a three-dimensional null point, he reports that there appears to be no significant heating associated with the null point. It may be that the heating at our null and its associated separatrix is transient and highly nonuniform, allowing the separatrix to be seen in C IV, as in this image. We identify the feature S as a separatrix because of its location, shape, and apparent height and evolution, as seen in the C IV movie.

3.2. Scenario of Flare Evolution

In Figure 4 *TRACE* C IV images of the key events associated with the X3 flare are shown. The impulsive phase of the flare begins at 20:02 UT. However, in the preflare stage there are

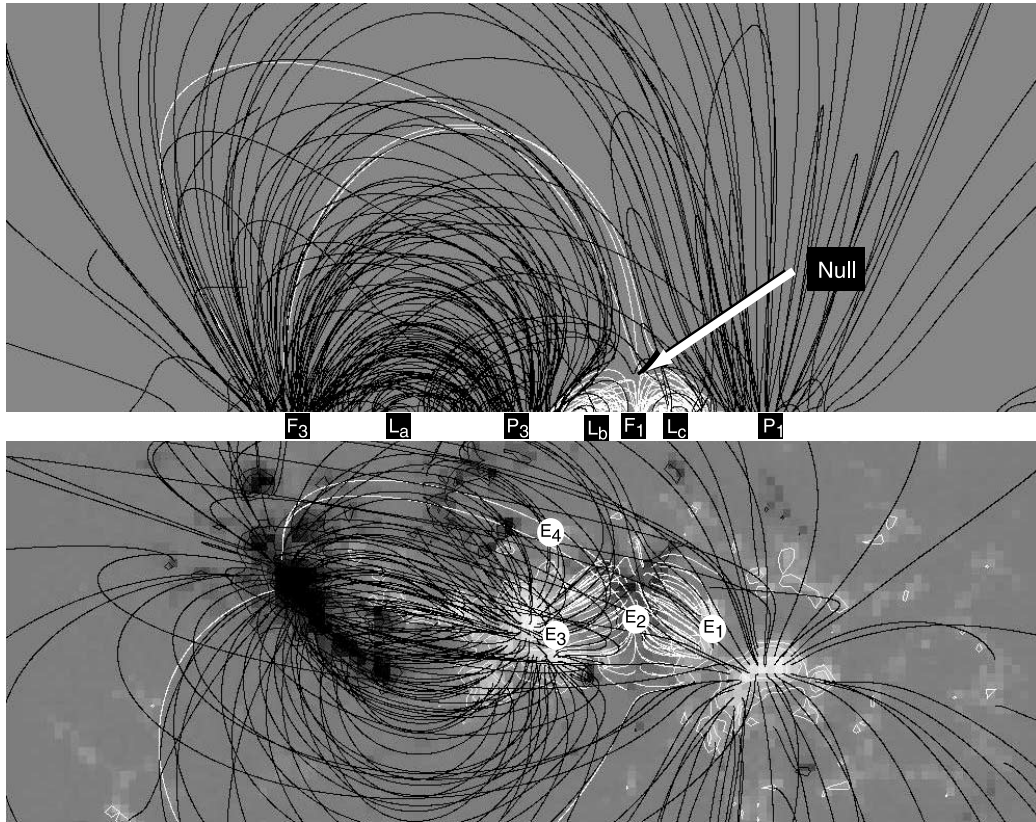


FIG. 7.—Side view and top view of the potential field computed from an MDI magnetogram. The white set of field lines is associated with the negative flux F_1 . The outer extremities of this set of field lines define the separatrix cupola. The small magnetic delta dipole (P_2 and F_2) hardly perturbs the overall quadrupolar field. The height in the side view is 140 Mm. At this height the plasma β is ~ 1 (Gary 2001). Hence, the magnetic field is influenced by the (unknown) upper boundary conditions, and this current-free field calculation models only the general connectivity to be expected, i.e., the topology. The helicity, the exact conjugate footpoints, and the upper boundary conditions of the region are not modeled.



FIG. 8.—*Left*: Enlargement of the *TRACE* image at 20:28:41 UT extracted from Fig. 3. The separatrix feature seen here is in the Y-null in the wake of the second eruption. (A separatrix refers to a magnetic surface across which linkage of the field lines is discontinuous.) This region filled with material in the eruption leading to the two flare ribbons, seen here below the separatrix. *Right*: Set of field lines defining the separatrix.

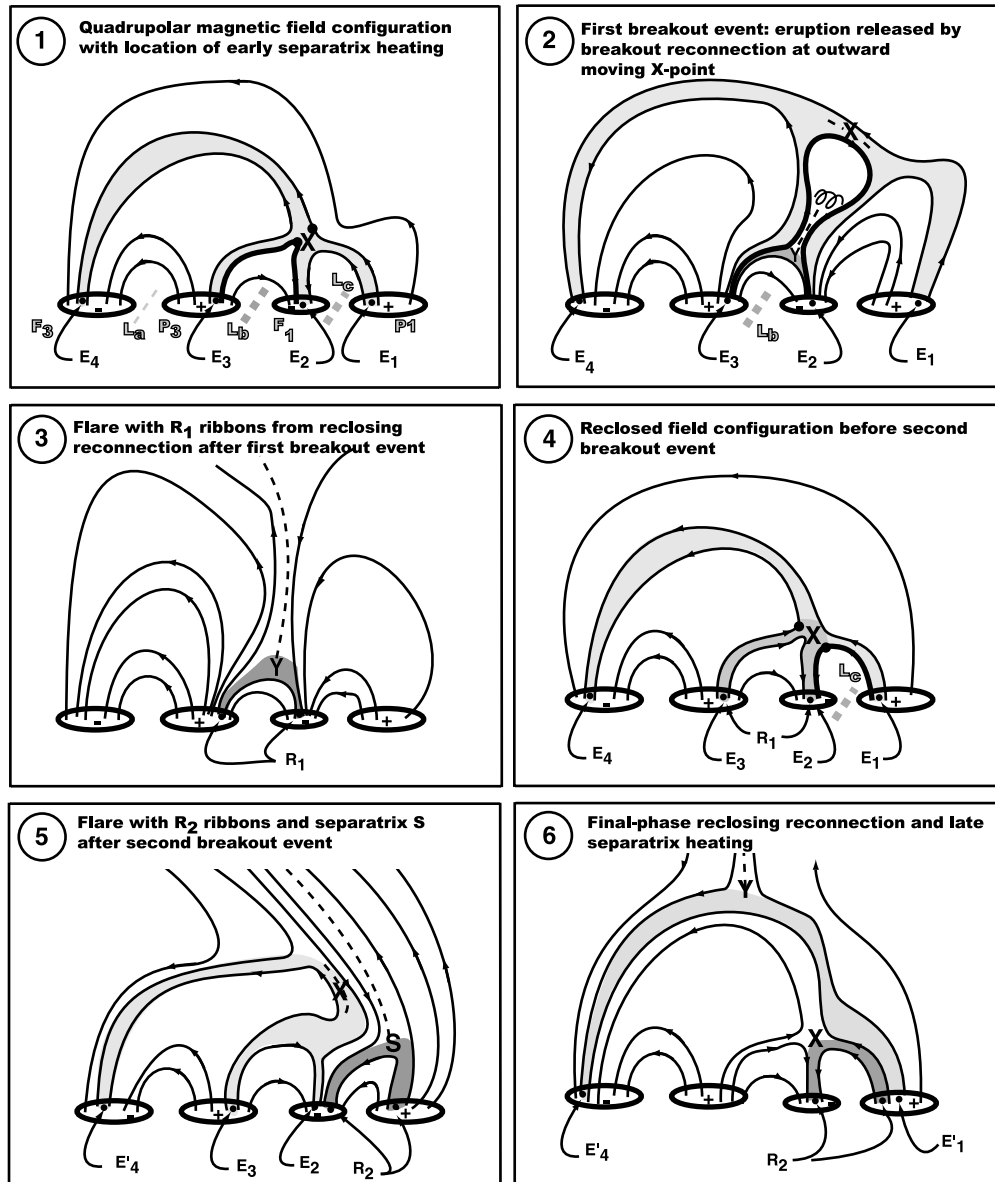


FIG. 9.—Topological sketches of the main components of the eruption, shown in cross section for the quadrupolar sunspot configuration of AR 10030. These six panels represent the magnetic field configuration at times near or between the times of the *TRACE* images of Fig. 4. In panel 1 the preflare magnetic field configuration is shown for $t \sim 19:50$ UT. The X-point null is the site of the initial breakout reconnection that unleashes the eruption of the sheared field along the neutral line L_b . The dots at this X-point indicate which field lines are reconnecting. In panel 2 the first breakout eruption is seen at $t \sim 20:05$ UT. In panel 3 the flare ribbons R_1 are shown with the associated open field lines at $t \sim 20:10$ UT. In panel 4 the reclosed field is shown with filled circles for the next breakout reconnection, shown near the X-point at $t \sim 20:15$ UT. Panel 5 shows the flare ribbons R_2 associated with the field closing behind the second breakout event. In panel 6 the final phase of the reclosing is shown at $t \sim 20:41$ UT, with the emission at E'_1 and E'_4 from the reconnection above the Y-point. These illustrations show the flux F_1 larger than in actuality to make the X-point null above the region more obvious.

small brightenings that we identify as four separatrix footpoints (Fig. 4, *top left*). At 19:49:58 UT, the emission at E_1 , E_2 , E_3 , and E_4 is at the locations of separatrix footpoint sites connected to the null above F_3 (see Figs. 7 and 9). Slow breakout reconnection is beginning at the null. At 20:02:53 UT the separatrix emission at E_1 , E_2 , E_3 , and E_4 is now brighter from the particles and heat from the fast reconnection of the outbreak. In $H\alpha$ at 20:03:55 UT and in $C\text{ IV}$ at 20:05:02 UT (Fig. 4), the pair of flare ribbons R_1 across the sheared neutral line L_b is growing. These flare ribbons are heated from internal reconnection in the wake of the erupting helix. The eruption of the helix and the reconnection below it are consequences of the external breakout reconnection, which allows the sheared core field to erupt and reconnect internally. At

20:28:01 UT a second eruption is producing the two flare ribbons R_2 across the sheared neutral line L_c . This eruption is released by a second episode of breakout reconnection at the null. This breakout reconnection begins once the reclosing and reforming reconnection of the first eruption sufficiently erodes the envelope of the field in which the sheared core field along L_c resides. At 20:28:41 UT, an upper atmospheric coronal separatrix (S) is seen filled with the material released by the eruption over L_c . At 20:41:56 UT the reconnection reclosing of the field opened by the second eruption produces the brightenings at E'_1 and E'_4 , near the former separatrix feet E_1 and E_4 .

In Figure 9 six stages of the scenario for the double-flare, double-CME event of July 15 are shown. In Figure 9 (*panel 1*),

the preflare, stressed, quadrupolar magnetic field configuration is illustrated with magnetic field concentrations P_1 , F_1 , P_3 , and F_3 , the separatrix foot locations E_1 , E_2 , E_3 , and E_4 , the sheared-field neutral lines L_a , L_b , and L_c , and the X-type neutral point. In this panel the two dots indicate which field lines are next to be reconnected as the stressed field (*thick field line*) over L_b pushes outward. The slow reconnection at the X-point feeds energy to heat the separatrix feet. The points E_1 – E_4 are the intersections of the separatrices (*light gray shading*) with the photosphere. The magnetic topology shown here has been simplified; as seen in Figure 4, the E_4 emission is outside the plane shown, and its connection to the null might be better represented by a spine of field lines (e.g., Aulanier et al. 2000; Lau & Finn 1990). The configuration of Figure 9 (*panel 1*) is for the time of $\sim 19:50$ UT, and the times for the other panels are near or between the times of the *TRACE* images in Figure 4.

As the magnetic field evolves through stress relief above the neutral line L_b , progression of the reconnection at the X-point and the resulting expansion of the sheared core field move the X-point upward. As the process proceeds the separatrix emission increases. Following Antiochos (1998), breakout reconnection transfers flux to the two sidelobes of the quadrupole, removes the confining field, and thus unleashes the sheared core field in an eruption. The breakout high over L_b either allows the preformed helix to erupt or allows the helix to form and erupt via internal reconnection, as illustrated in Figure 9 (*panel 2*). The opening of the quadrupolar field by this breakout eruption is confirmed by the first CME. The reclosing reconnection along the current sheet above the Y-point null in Figure 9 (*panel 3*) powers the two-ribbon flare R_1 across the neutral line L_b . This reclosing reconnection also powers the second and third microwave spikes and produces the first maximum in the soft X-ray flux.

In Figure 9 (*panel 4*) the reclosed field configuration is shown well after the first breakout but before the second breakout event. The second breakout event is produced by the expanding stressed field over L_c . The dots at the X-point in this panel show the reconnection direction for this second breakout, which follows a similar, but not identical, scenario to that of Figure 9 (*panel 2*). Because of the stressed magnetic field and the overlying magnetic loops removed by reconnection in the aftermath of the first breakout event, the flux over L_c expands outward. Before the first breakout the stressed field across L_b affects the stressed field across L_c . Following the reclosing, after the first breakout, the stressed field over L_c is now allowed to expand and reconnect across the X-point in Figure 9 (*panel 4*). With rapid reconnection on the east side of the expanding breakout, the stressed flux associated with L_c erupts outward, forming a current sheet behind and a current sheet on its east side. The result of this eruption is the configuration of Figure 9 (*panel 5*). This breakout eruption is manifested by the fourth microwave burst r_4 at 20:24 UT, the second filament eruption, and the beginning of the second two-ribbon flare (R_2). The opening of the quadrupolar field for the second time, i.e., the second breakout, is confirmed by a second and faster CME. The second CME is faster perhaps because of a weakened field configuration resulting from the first breakout. As this configuration relaxes, the inverted-Y separatrix above F_3 is seen in the *TRACE* images at 20:28 UT (Fig. 8.) The feature S is formed by reclosing after the lateral breakout, which is not the same as the reclosing after the first breakout. (In any case, at C IV temperatures, the *TRACE* movie shows no such feature in the reclosing of the first breakout eruption.) The final-phase reclosing reconnection is shown in

Figure 9 (*panel 6*). This final reclosing reconnection above the late-phase high Y-point null produces the heating for E'_1 and E'_4 , which is seen in Figure 4 (*bottom right*) at 20:41:56 UT.

3.3. Formation and Eruption of the Helix

To illustrate that the erupting feature in the *TRACE* C IV images is a helical flux tube, a simple three-turn helix was modeled to simulate the observed aspect and expansion. The results, shown as insets in Figure 1, reproduce the helical structure. The geometry of this model was specified using the fact that, at the time of the erupting helix, AR 10030 was located at $N22^\circ$, $E01^\circ$ and, in the image plane, the helix's associated neutral line (L_b ; Fig. 2) made an angle of $\sim 22^\circ$ with a north-south line. Furthermore, defining the helix velocity vector as the time rate of change of the displacement vector of the center of the helix, then, in the image plane, the velocity vector is tilted up 41° from the east-west constant-latitude line. Using this angle and assuming that the helix velocity vector is perpendicular to the associated magnetic neutral line, the plane of the rising helix (as defined by the helix center line and its footpoints) is calculated to be tilted 36° from the local heliographic vertical.

The tether-cutting concept is at the heart of the standard model for EFs as first proposed by Hirayama (1974) and extended recently by Moore et al. (2001). The concept is that reconnection begins low in the sheared core of a magnetic arcade. This tether-cutting reconnection progressively transfers magnetic shear from lower to higher in the arcade, producing a growing twisted flux tube and unleashing it for eruption. This configuration is normally assumed to be responsible for the sigmoid-shaped X-ray signatures. Antiochos & DeVore (1999) state that there are no three-dimensional simulations that show evidence of such tether-cutting reconnection, nor is there evidence that rapid tether-cutting reconnection in the standard model is the initiator of CMEs/EFs. The alternative model for the EF trigger, the breakout model (Antiochos 1998; Antiochos et al. 1999), is consistent with the flare evolution. The key features of this model are (1) multipolar configuration, (2) photospheric shearing, and (3) rapid reconnection *high* in the corona. The important distinction is that the breakout model trigger or magnetic destabilization is by external reconnection high in the corona and not within the stressed core field. Therefore, the global magnetic field and a higher plasma β are more important than in the standard model.

The helix is formed in a strongly sheared magnetic field along the neutral line L_b . It is quite possible that the helix is formed before it erupts, with its formation following the development of the three-dimensional MHD simulation described by DeVore & Antiochos (2000), since the birth site of the helix is a progressively sheared magnetic field. Because the overall active region is evolving with the moving magnetic elements pouring out of sunspot P_3 , the subregion along L_b has the necessary character for continuing shear buildup. A sheared-core arcade field, through gradual internal reconnection, becomes a multiple-turn helix straddling the neutral line envisioned in the DeVore & Antiochos (2000) model. This pre-eruption sheared field with a filament and helical core remains stable until the overlying field is sufficiently weakened by the external breakout reconnection, and then it erupts and produces a CME.

The results of the velocity calculations for the erupting helix are shown in Figure 10. The transverse velocity motion across the image plane (*upper solid curve*) initially has a constant acceleration (*dash-dotted line*) of $\sim 25 \text{ km s}^{-2}$. The

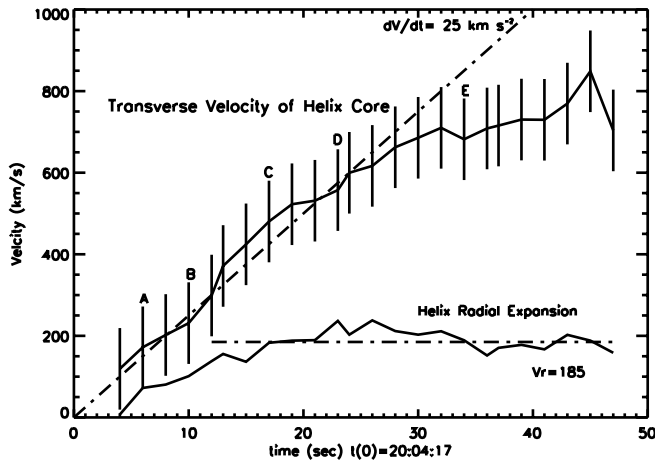


FIG. 10.—Velocity profiles of the erupting helix. The transverse velocity (upper solid curve), as seen in the image plane, initially has a constant acceleration (dash-dotted line) of $\sim 25 \text{ km s}^{-2}$. The measured transverse velocity is that of the top of the core of the helix. The radial expansion of the helix from its core has a velocity of $\sim 185 \text{ km s}^{-1}$ after about 15 s. The radial expansion was measured using the average semidiameter of the main turns. Linear extrapolation of the transverse velocity to zero gives an onset time of $t(0) = 20:04:17 \text{ UT}$. The times of the first five images of Fig. 1 are marked A–E. At the time of each image, the vertical lines are the error (200 km s^{-1}) associated with the transverse velocity; the helix expansion velocity has the same uncertainty.

transverse velocity was obtained from measurements of the displacements of the apex of the core of the helix. The radial expansion of the helix from its core has a velocity of $\sim 185 \text{ km s}^{-1}$ after about 15 s. The radial expansion was measured using the average semidiameter of the main turns. Linear extrapolation of the transverse velocity to zero gives an onset time of $t(0) = 20:04:17 \text{ UT}$. This is approximately the start of the fast phase of the eruption of the helix seen in the full sequence of frames of the event. The times of the first five images of Figure 1 are marked A–E in Figure 10. At the time of each image, the vertical lines are the error (200 km s^{-1}) associated with the transverse velocity; the helix expansion velocity has the same uncertainty.

The characteristics of the helix in terms of its transverse and radial velocity are given in Figure 10. We now compare the observed erupting velocities with the Alfvén speed, the propagation speed of magnetic disturbance. The maximum transverse velocity perpendicular to the line of sight is 800 km s^{-1} , while the maximum radial expansion is 185 km s^{-1} . From the geometry, the velocity is tilted at $\sim 45^\circ$ away from the image plane; hence, the helix velocity is $\sim 1100 \text{ km s}^{-1}$, and the helix’s estimated height is $\sim 9000 \text{ km}$ after 30 s. The 1967 Newkirk model gives a density at this height of $N_e = 10^{8.89} \text{ cm}^{-3}$ (Mann et al. 2000); using $B = 22 \text{ G}$, the Alfvén velocity is $V_A \sim 1500 \text{ km s}^{-1}$. The speed estimates of the helix and the CMEs are physically consistent with this Alfvén speed. Furthermore, assuming that the plasma in the helix is propelled by the magnetic field, and equating the magnetic energy density $B^2/8\pi$ and the kinetic density $(1/2)mv^2$, one obtains an estimate of the magnetic field strength of $B = 4.5 \times 10^{-12} v n \text{ G}$ (Tandberg-Hanssen et al. 1980). For a velocity of 500 km s^{-1} and particle density of $n = 10^{10} \text{ cm}^{-3}$, the estimated magnetic field of 20 G is consistent with the values of the Alfvén velocities. The conclusion of these estimates is that the observed velocities have reasonable magnitudes and are consistent with the observed strength and configuration of the magnetic field. Furthermore,

the observed rapid escape of the helix is entirely consistent with the breakout scenario.

4. SUMMARY AND DISCUSSION

The relation between core-field tether cutting and global magnetic ballooning via breakout in initiating magnetic eruption is answered for the case studied. The specific timing of the eruption of a core field is seen from *TRACE* images, which capture the eruption of the core field helix. This eruption begins after the initiation of the flare. In addition, an ejection of twisted prominences has been reported by Kurokawa et al. (1987); they reported $H\alpha$ observations of a helical eruption. This helical eruption is similar to the *TRACE* helix in that the eruption is after the impulsive phase of the flare and is from a sheared magnetic field. Over a period of 22 minutes, a highly twisted helical filament is seen to erupt and untwist from the delta sunspot configuration, after the X3 flare. The impulsive phase started 4 minutes before the filament started to erupt. This example also suggests that the standard model must be in error for the initiation of this flare.

The importance of our observations and the Kurokawa et al. (1987) observations is that they distinguished between the two competing models. Our observations support the breakout model over the standard model for the initiation of the X3 flare of 2002 July 15 (20:02 UT). First, our observations show that the strong eruptive phase of the sheared helix core of the stressed magnetic field begins after the flare impulsive phase has started. This is in conflict with the standard model and supports the breakout model. Second, the initial brightenings are distant from the neutral lines and agree with reconnection at the null, being located appropriately for the remote footpoints of the separatrix. Third, the magnetic field is a complex quadrupolar field that is undergoing evolution. There are several other important points to make in regards to the breakout model and our observations. Antiochos et al. (1999) make the case that the energy for CMEs must be stored in the stressed magnetic field of a multiple-flux system. The quasi-static evolution of the stressed magnetic field is driven by the displacement of magnetic footpoints and the emergence-submergence of magnetic flux. The MDI movie of the complex AR 10030 shows such strong activity in the photospheric magnetic flux distribution. Within the model, the sheared field expands outward and pushes overlying flux (and the null point) outward. AR 10030 is indeed highly stressed, as shown by the MSFC vector magnetograms. Gary (2001) points out that the plasma β begins to increase and approach 1 at relatively low coronal heights (100 Mm) over active regions, i.e., the force-free region is rather low in the corona. This implies that the plasma at the X-point can inhibit the onset of reconnection until the current sheet becomes very thin. Also important to the breakout model is that much of the flux of the central and overlying systems remain closed. This is consistent with the X3 flare. In the breakout model, intense current sheets form late in the shearing; this is consistent with the observation of highly sheared magnetic fields for hours before flare onset. From the timing of the two eruptions from the two neutral lines L_b and L_c and the timing of the two CMEs, the plasma within the two CMEs must come from the eruptions associated with the two double-ribbon flares. However, the most decisive observation is that the initial impulsive phase occurred before the first core eruption.

In conclusion, we feel that these observations show that the standard model for the initiation of EFs does not apply to all ejective flares. However, the upper reconnection site of the

breakout has yet to be directly observed. The trigger site of flares is still elusive.

We would like to thank Steve Suess and Guillaume Aulanier for their helpful comments and suggestions that improved this paper. This work was funded by the NASA Office of Space Science through the Solar Physics Supporting Research and Technology program. The *SOHO* LASCO data used here were produced by a consortium of the Naval Research Laboratory (USA), the Max-Planck-Institut für Aeronomie (Germany), the Laboratoire d'Astronomie (France), and the University of Birmingham (UK). *SOHO* is a project of international cooperation between ESA and NASA. *TRACE* is operated jointly

out of the Goddard Space Flight Center by scientists from the University of Chicago, Montana State University, Lockheed-Martin Solar and Astrophysical Laboratory, and Harvard-Smithsonian Center of Astrophysics. The *SOON* and *GOES* data are from the Space Environment Center, Boulder, CO, National Oceanic and Atmospheric Administration, Department of Commerce. MDI is a project of the Stanford-Lockheed Institute for Space Research and is a joint effort of the Solar Oscillations Investigation in the W. W. Hansen Experimental Physics Laboratory of Stanford University and the Solar and Astrophysics Laboratory of the Lockheed-Martin Advanced Technology Center. The Big Bear Solar Observatory and OVSA are maintained and operated by the Center for Solar Research at the New Jersey Institute of Technology.

REFERENCES

- Alissandrakis, C. E. 1981, *A&A*, 100, 197
 Amari, T., Luciani, J. F., Aly, J. J., Mikic, Z., & Linker, J. 2003, *ApJ*, 595, 1231
 Amari, T., Luciani, J. F., Aly, J. J., Mikic, Z., & Tagger, M. 1996, *ApJ*, 466, L39
 Amari, T., Luciani, J. F., Mikic, Z., & Linker, J. 1999, *ApJ*, 518, L57
 Antiochos, S. K. 1998, *ApJ*, 502, L181
 Antiochos, S. K., & DeVore, C. R. 1999, in *Sun-Earth Plasma Connections*, ed. J. L. Burch, R. L. Carovillano, & S. K. Antiochos (Geophys. Monogr. 109; Washington, DC: AGU), 113
 Antiochos, S. K., DeVore, C. R., & Klimchuk, J. A. 1999, *ApJ*, 510, 485
 Anzer, U., & Tandberg-Hanssen, E. 1970, *Sol. Phys.*, 11, 61
 Aulanier, G., DeLuca, E. E., Antiochos, S. K., McMullen, R. A., & Golub, L. 2000, *ApJ*, 540, 1126
 Birn, J., & Schindler, K. 1981, in *Solar Flare Magnetohydrodynamics*, ed. E. Priest (New York: Gordon & Breach), 337
 Brekke, P., Rottman, G. J., Fontenla, J., & Judge, P. G. 1996, *ApJ*, 468, 418
 Cuny, Y. 1971, *Sol. Phys.*, 16, 293
 Dere, K. P., Brueckner, G. E., Howard, R. A., Michels, D. J., & Delaboudiniere, J. P. 1999, *ApJ*, 516, 465
 DeVore, C. R., & Antiochos, S. K. 2000, *ApJ*, 539, 954
 Falconer, D. A., Moore, R. L., & Gary, G. A. 2002, *ApJ*, 569, 1016
 Filippov, B. 1999, *Sol. Phys.*, 185, 297
 Forbes, T. G., & Priest, E. 1995, *ApJ*, 446, 377
 Gary, D. E. 2000, in *ASP Conf. Ser. 206, High Energy Solar Physics Anticipating HESSI*, ed. R. Ramaty & N. Mandzhavidze (San Francisco: ASP), 297
 Gary, G. A. 2001, *Sol. Phys.*, 203, 71
 Gary, G. A., & Alexander, D. 1999, *Sol. Phys.*, 186, 123
 Gary, G. A., & Moore, R. L., Hagyard, M. J., & Haisch, B. M. 1987, *ApJ*, 314, 782
 Hagyard, M., Low, B. C., & Tandberg-Hanssen, E. 1981, *Sol. Phys.*, 73, 257
 Hagyard, M. J., Adams, M. L., Smith, J. E., & West, E. A. 2000, *Sol. Phys.*, 191, 309
 Hagyard, M. J., Gary, G. A., & West, E. A. 1998, *The SAMEX Vector Magnetograph* (NASA TM-4048; Washington, DC: NASA)
- Hagyard, M. J., Stark, B. A., & Venkatakrishnan, P. 1999, *Sol. Phys.*, 184, 133
 Handy, B. N., Bruner, M. E., Tarbel, T. D., Title, A. M., Wolfson, C. J., Laforge, M. J., & Oliver, J. J. 1998, *Sol. Phys.*, 183, 29
 Handy, B. N., et al. 1999, *Sol. Phys.*, 187, 229
 Hirayama, T. 1974, *Sol. Phys.*, 34, 323
 Hood, A. W., & Priest, E. R. 1980, *Sol. Phys.*, 66, 113
 Kurokawa, H., Hanaoka, Y., Shibata, K., & Uchida, Y. 1987, *Sol. Phys.*, 108, 251
 Lau, Y.-T., & Finn, J. M. 1990, *ApJ*, 350, 672
 Lionello, R., Mikic, Z., Linker, J. A., & Amari, T. 2002, *ApJ*, 581, 718
 Liu, Y., Jiang, Y., Ji, H., Zhang, H., & Wang, H. 2003, *ApJ*, 593, L137
 Maia, D., Aulanier, G., Wang, S. J., Pick, M., Malherbe, J.-M., & Delaboudiniere, J.-P. 2003, *A&A*, 405, 313
 Mann, G., Aurass, H., Klassen, A., Estel, C., & Thompson, B. J. 2000, in *8th SOHO Workshop on Plasma Dynamics and Diagnostics in the Solar Transition Region and Corona*, ed. J.-C. Vial & B. Kaldeich-Schumann (ESA SP-446; Noordwijk: ESA), 477
 Moore, R. L., Sterling, A. C., Hudson, H. S., & Lemen, J. R. 2001, *ApJ*, 552, 833
 Priest, E. R., & Milne, A. M. 1980, *Sol. Phys.*, 65, 315
 Qiu, J., Ding, M. D., Wang, H., Denker, C., & Goode, P. R. 2000, *ApJ*, 544, L157
 Ronan, R. S., Orrall, F. Q., Mickey, D. L., West, E. A., Hagyard, M. J., & Balasubramaniam, K. S. 1992, *Sol. Phys.*, 138, 49
 Rust, D. M., & Kumar, A. 1996, *ApJ*, 464, L199
 Scharmer, G. B., Gudiksen, B. V., Kiselman, D., Löfdahl, M. G., & Rouppe van der Voort, L. H. M. 2002, *Nature*, 420, 151
 Scherrer, P. H., et al. 1995, *Sol. Phys.*, 162, 129
 Secchi, P. A. 1870, *Le Soleil* (Paris: Gauthier Villars)
 Sterling, A. C., Moore, R. L., Qiu, J., & Wang, H. 2001, *ApJ*, 561, 1116
 Sturrock, P. A., Kaufmann, P., Moore, R. L., & Smith, D. F. 1984, *Sol. Phys.*, 94, 341
 Tandberg-Hanssen, E., Martin, S. F., & Hansen, R. T. 1980, *Sol. Phys.*, 65, 357
 van Ballegooijen, A. A., & Martens, P. C. H. 1989, *ApJ*, 343, 971
 ———. 1990, *ApJ*, 361, 283